Wind and Structures, *Vol. 30, No. 4 (2020) 433-450*
DOI: https://doi.org/10.12989/was.2020.30.4.433

Wind-sand coupling movement induced by strong typhoon and its influences on aerodynamic force distribution of the wind turbine

Shitang Ke*, Yifan Dong[a], Rongkuan Zhu[b] and Tongguang Wang[c]

Jiangsu Key Laboratory of Hi-Tech Research for Wind Turbine Design, Nanjing University of Aeronautics and Astronautics, Nanjing 210016, China

(Received August 27, 2019, Revised December 30, 2019, Accepted January 23, 2020)

Abstract. The strong turbulence characteristic of typhoon not only will significantly change flow field characteristics surrounding the large-scale wind turbine and aerodynamic force distribution on surface, but also may cause morphological evolution of coast dune and thereby form sand storms. A 5MW horizontal-axis wind turbine in a wind power plant of southeastern coastal areas in China was chosen to investigate the distribution law of additional loads caused by wind-sand coupling movement of coast dune at landing of strong typhoons. Firstly, a mesoscale Weather Research and Forecasting (WRF) mode was introduced in for high spatial resolution simulation of typhoon "Megi". Wind speed profile on the boundary layer of typhoon was gained through fitting based on nonlinear least squares and then it was integrated into the user-defined function (UDF) as an entry condition of small-scaled CFD numerical simulation. On this basis, a synchronous iterative modeling of wind field and sand particle combination was carried out by using a continuous phase and discrete phase. Influencing laws of typhoon and normal wind on moving characteristics of sand particles, equivalent pressure distribution mode of structural surface and characteristics of lift resistance coefficient were compared. Results demonstrated that: Compared with normal wind, mesoscale typhoon intensifies the 3D aerodynamic distribution mode on structural surface of wind turbine significantly. Different from wind loads, sand loads mainly impact on 30° ranges at two sides of the lower windward region on the tower. The ratio between sand loads and wind load reaches 3.937% and the maximum sand pressure coefficient is 0.09. The coupling impact effect of strong typhoon and large sand particles is more significant, in which the resistance coefficient of tower is increased by 9.80% to the maximum extent. The maximum resistance coefficient in typhoon field is 13.79% higher than that in the normal wind field.

Keywords: large wind turbine system; typhoon; WRF mode; mesoscale/small-scale coupling; wind-sand coupling movement; aerodynamic distribution

1. Introduction

China possesses a long coastline and rich exploitable offshore wind power resources. Compared with onshore wind power, offshore wind power has higher average wind speed and more hours of power utilization (Sun *et al*. 2012). However, there are tough weather conditions in coastal regions and frequent occurrences of strong typhoon. It is common to have wind-induced damages of large wind turbine (Utsunomiya *et al*. 2013, Wang *et al*. 2013). In addition, strong turbulence of typhoon is another high-powered influencing factor of formation and evolution of coast dunes (Dissanayake *et al*. 2015, Karunarathna *et al*. 2018). Driven by wind field in near-ground boundary layer (Bagnold 1935, Bagnold, 1937), sand particles may move randomly in a certain range of height. Sand particles and wind field develop mutual coupling effect and energy migration, so that sand particles impact on the surface of wind turbine at a large speed, thus forming additional loads and wind erosion effect (Jiang *et al*. 2010). Such additional loads and wind erosion effect influence the safety performance and service life of wind turbine significantly (Zhang *et al*. 2016). Therefore, theoretical studies on gas-solid flows has important engineering significance and theoretical values to discuss the action mechanism of different sizes of sand particles on aerodynamic loads of wind turbine under wind-sand coupling movement induced by strong typhoon.

Many studies on wind turbine under typhoon effect have been reported. Takeshi *et al*. (2005) investigated effects of relative positions of blade, wind direction and doorway on collapse of wind turbine according to the wind turbine collapse data and measured typhoon speed in Japan. Wang *et al*. (2013) and Luo *et al*. (2016) carried out a systematic analysis on wind-induced static/dynamic responses of tower of the wind turbine under the typhoon effect by combining theoretical deduction and pulsation wind spectra. Besides, they offered some suggestions to the anti-typhoon tower design of the tower turbine. Lian *et al*. (2016) analyzed aerodynamic load characteristics of blades of wind turbine under typhoon effect systematically by combining theoretical analysis and measured typhoon data, and constructed an anti-typhoon design optimization model of

*Corresponding author, Professor
E-mail: keshitang@163.com
[a]Postgraduate
E-mail: yfdongnuaa@163.com
[b]Postgraduate
E-mail: zhurongkuannuaa@163.com
[c]Professor
E-mail: tgwang@nuaa.edu.cn

http://www.techno-press.com/journals/was&subpage=7
ISSN: 1226-6116 (Print), 1598-6225 (Online)

aerodynamic blade shape of wind turbines. Existing researches on responses of coast dunes to strong typhoon mainly focus on erosion, transportation and stacking mechanisms. Pye K *et al*. (2016) pointed out that height of the coast dune in Sefton in the northwest of England was decreased by 12 m after the landing of a strong storm. Priestas *et al*. (2010) measured that the dune volume on St. George Island was decreased by about 7% by the hurricane “Dennis” in 2005. By comparing area, position and morphological data of different dune types before and after hurricanes, Pries *et al*. (2008) analyzed erosion effects of hurricane on coast dune on the Santa Rosa Island in the Gulf of Mexico. To sum up, researches on resistance of wind turbine against strong typhoon mainly concern one-way effect of typhoon (in 2011, Chou and Tu 2011), but haven’t analyze the additional load effect of large-scaled durable wind-sand coupling movement of coast dune on the structure at the landing of strong typhoons (Chen *et al*. 2012). Li *et al*. (2017) discovered from a wind tunnel test that the sand-wind collaborative effect can increase base shear of low buildings. Zhang *et al*. (2016) studied the erosive wearing behavior of wind turbine blades in wind-sand environment under different speeds and impact angles through a low-angle accelerating abrasion test. They found that erosive wearing of blade coating increased with the increase of erosion rate. In a word, the influences of wind-and environment on aerodynamic performances of wind turbine cannot be ignored. In particular, quantitative and qualitative studies on wind-sand coupling effect of large wind turbine system under strong typhoon are needed. In fact, analyzing aerodynamic force of wind turbine in wind-sand coupling environment induced by strong typhoon must consider time-variant characteristics throughout the mesoscale typhoon process and structural characteristics of wind turbine under small-scale typhoon.

In this study, a high temporal-spatial resolution simulation of typhoon “Megi” was carried out by using the mesoscale Weather Research and Forecast (WRF) mode. The wind speed profile in the simulation region was gained based on nonlinear least square fitting after analysis of typhoon field information. On this basis, a normal wind speed profile was set at the same height of type-A landform with the typhoon speed profile. Meanwhile, the discrete phase model (DPM) was added into the Computational Fluid Dynamics(CFD)to realize two-phase coupling (Zhao *et al*. 2016, Xin *et al*. 2018, Gao *et al*. 2018) with the incoming air. Wind-sand coupling movement characteristics and aerodynamic distribution on a 5MW horizontal axial wind turbine in a wind field in southeastern coast of China under strong typhoon and normal wind conditions were studied.

2. Mesoscale typhoon field simulation and result analysis

2.1 Selection of WRF mode

WRF (Skamarock *et al*. 2008) mode is a mesoscale weather research and forecast system which is developed by NCAR, NOAA and Rainstorm Analysis and Forecast Center of Oklahoma University. Since wind characteristics of typhoon boundary layer are different from the normal climate mode, evident temporal-spatial variations and multi-scale eddy structure will be developed during the typhoon process (Song *et al*. 2012, Li *et al*. 2015). The mesoscale WRF mode based on dynamics and thermodynamics of fluid can not only simulate the wind speed field and wind temperature field of typhoon effectively, but also consider evolution process, strong variation and attenuation characteristics of typhoon comprehensively (Wyszogrodzki *et al*. 2012). The sphere of influence of typhoon reaches hundreds of kilometers. Therefore, the grid resolution of a typhoon field is generally at the kilometer magnitude. However, the overall size of large wind turbine is “only” hectometer magnitude, showing a great scale difference with the typhoon scale. Moreover, it has to go deep into the flange boundary layer in order to predict aerodynamic loads of blade edge accurately. The grid size at near wall is generally lower than 10-2 m. To realize wind-sand coupling movement under strong typhoon conditions, WRF mode on this magnitude is completely failed. Therefore, the mesoscale/small-scaled embedded WRF/CFD has to be applied for high-precision simulation of multi-scale two-phase flow field in a large wind turbine system considering movement of sand particles. Besides, high-precision transmission of parameters and flowing structure, multi-layer and multi-scale grid embedding, multi-time scale control and cross-scale mutation are solved (Maruyama *et al*. 2010).

In the present study, the WRF-ARW (Skamarock *et al*. 2008) mode based on non-static equilibrium Euler equation model was applied. In the WRF-ARW mode, the horizontal direction used Arakawa C grids and the vertical direction used the terrain following quality coordinate system which can be transferred on the Linux system. With considerations to influences of physical processes (e.g., water vapor, long-wave and short-wave radiations, cumulus cloud and underlying), the WRF-ARW mode can reasonably simulate airflow, air pressure and wind field characteristics in a large area. Simulation results are input as the boundary condition for CFD simulation.

2.2 Setting of WRF parameters

The Typhoon “Megi” was used as the simulation object in this study. “Megi” was the 13# typhoon which was developed on the northwest Pacific Ocean in 2010 and it was characteristic of large sphere of influence (141°E~117°E), high strength (17 level of maximum wind, the maximum wind speed is about 56.1 - 61.2 m/s) and long duration (from October 13th to 25th, 2010). A numerical simulation on typhoon route, air pressure field and wind speed field was carried out effectively. The simulation case covered the whole process from eastward moving the strong typhoon on 00:00 of October 22nd to the landing on 00:00 of October 24th.

Firstly, gridding of the WRF has to be performed: WRF mode is a complete compressible non-static mode and uses the Euler quality coordinates (η) along the terrain in the vertical direction (Fig. 1(a))

$$\eta = \left(p_h - p_{ht}\right)/\mu, \quad \mu = p_{hs} - p_{ht} \tag{1}$$

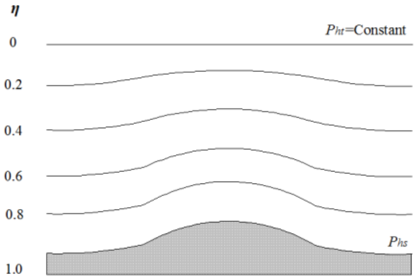

(a) Vertical grids

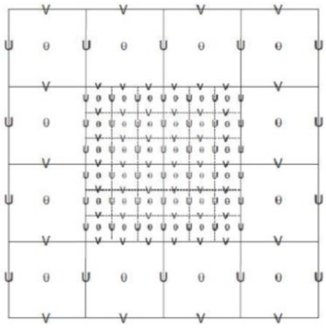

(b) Horizontal grids (thick/thin grid spacing ratio=3:1)

Fig. 1 Gridding program of the WRF mode

Where p_h is the air pressure at the target point, p_{ht} is the air pressure at the top layer and it is a constant. p_{hs} is the near-ground air pressure

The horizontal computational domain applied the Arakawa-C gridding (Fig. 1(b)). Arakawa-C grids can express scalar and vector simultaneously (Basso *et al*. 2014, Miglietta *et al*. 2013), which can increase accuracy of high-resolution simulation. However, scalar and vector occupy different positions on Arakawa-C grids. Components (u and v) of horizontal wind speed are defined at the orthogonal boundaries of the quadrilateral cell region. They are perpendicular to the vertical and longitudinal unit boundaries. Scalars like temperature, humidity and air pressure at in the center of quadrilateral cell region. Speed of Arakawa-C grids and other variables are all calculated on the single grid spacing, showing good frequency dispersion and conservativeness.

With comprehensive considerations to data demands and computing conditions, the typhoon field of WRF mode was calculated using the 3-layer one-way embedding scheme with horizontal resolutions of 13.5 km, 4.5 km and 1.5 km, respectively. The grid spacing (D01) and number of grids in the outer layer were 13.5km and 211×211, respectively. The grid spacing (D02) and number of grids in the second layer were 4.5 km and 217×217, respectively. The grid spacing (D03) and number of grids in the inner layer were 1.5km and 241×241, respectively. Lambert scheme was used for the map projection (Carvalho *et al*. 2014). WRF simulation region is shown in Fig. 2.

The wind turbine is at the lower high-turbulence region of the atmospheric boundary layer and it is influenced significantly by airflow quality, humidity and heat transmission of the boundary layer. Therefore, the physical scheme of parameterization has direct impacts on simulation accuracy of boundary layers in the typhoon field.

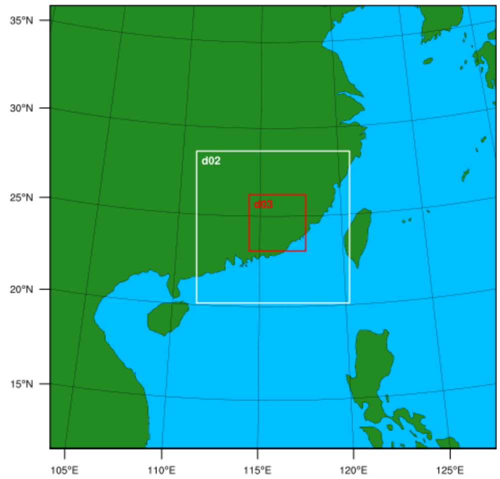

Fig. 2 WRF simulation region

Table 1 Setting of parameters in the WRF mode

WRF parameters	Primary zone d01	Nesting region d02	Nesting region d03
Number of nesting grids	211	217	241
Integral time step	180s	180s	180s
Short-wave radiation	RRTM scheme		
Long-wave radiation	Dudhai scheme		
Road process	Noah scheme		
Micro-physical scheme	Lin scheme		
Dynamic framework of WRF mode	ARW non-static		

The MYJ boundary layer scheme and KainFritsch cumulus convection parameterization scheme were determined after multiple screening tests, which were used in high-precise numerical simulation of "Megi" by 48 h. Simulation results provide boundary conditions for the follow-up downscaling operation of embedded CFD. Other parameters are listed in Table 1.

2.3 WRF simulation results

Wind field information during landing of typhoon was gained through WRF. To verify typhoon simulation, comparison between the simulated path of whole landing process of typhoon "Megi" and the measured path was supplemented (Fig. 3). Red line is the simulated path of WRF and blue line is the measured path of tropical cyclone data center of China Meteorological Administration. According to analysis, the overall landing path of typhoon "Megi" was slightly northward and the simulated path was relatively consistent with the measured path.

The WRF simulated wind field information in the typical altitude simulation region and the measured results when typhoon "Megi" landed at Xiang'an, Xiamen, on 00:00, October 24th. According to comparison between simulated results and measured results (Fig. 4), the maximum wind speed and wind pressure in Xiamen during the landing of typhoon "Megi" ranged 20 - 24 m/s and 940 - 960 hPa, respectively. The simulated results were similar with measured results (maximum wind speed=23 m/s and

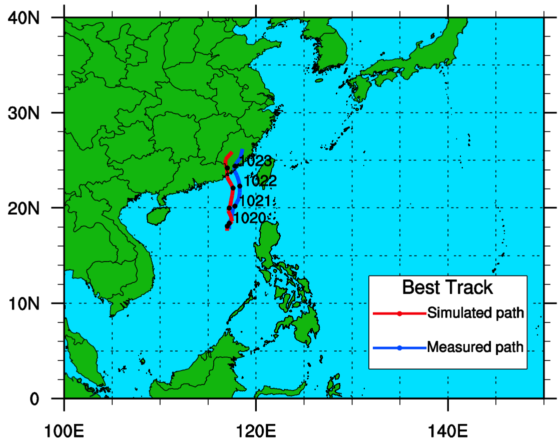

Fig. 3 Typhoon paths in the whole process of landing

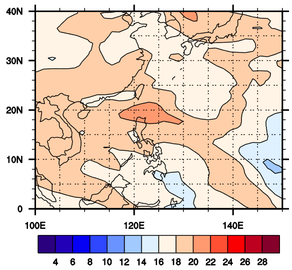

(a) Simulated wind speed

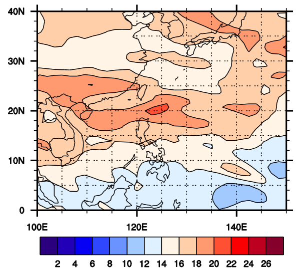

(b) Measured wind speed

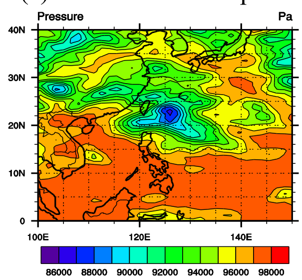

(c) Simulated wind pressure

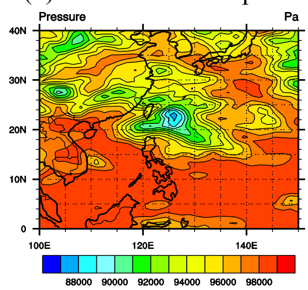

(d) Measured wind pressure

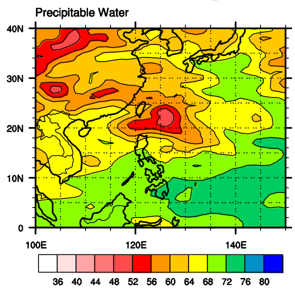

(e) Simulated precipitation

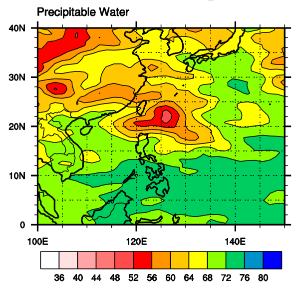

(f) Measured precipitation

Fig. 4 Output information of "Megi" typhoon field by WRF

pressure at center=980 hPa) of the typhoon website of National Meteorological Center of CMA. The maximum error was smaller than 12%. Cloud precipitation close to thetyphoon belongs to convective precipitation for a long time. The heavy precipitation in the study area was related with typhoon intensity and distance to the center. The Noah pavement process can simulate surface flux and airflow convergence field well. The simulated results conform well to measured results. The WRF simulated wind field information in the typical altitude simulation region and the measured results.

Wind speed profiles close to the typhoon center at different moments are shown in Fig. 5. According toanalysis, the near-ground typhoon speed is in regular distribution at different moments, but wind speed distribution at high altitude is disordered. In this process,

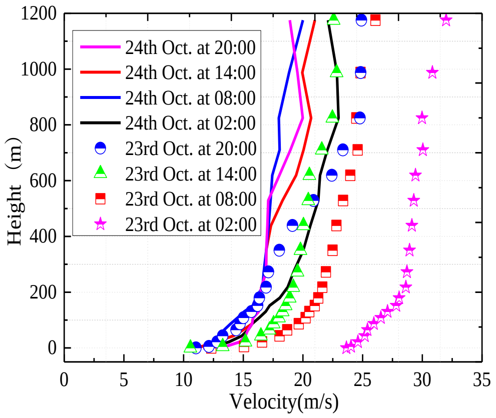

Fig. 5 Wind speed profile close to the typhoon center at different moments

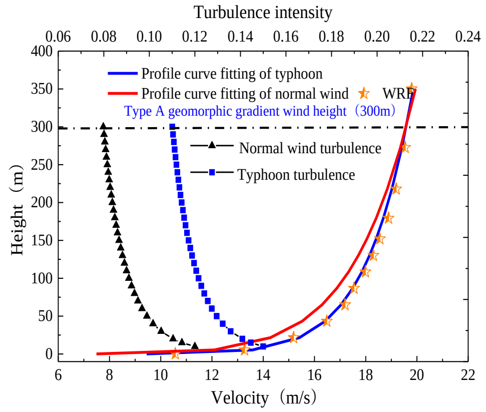

Fig. 6 Near-ground wind speed profile information in core region

typhoon intensity is transformed gradually from a tropical storm into a tropical depression. The fitting curves of near-ground typhoon speeds based on near-ground wind speed in the center of simulation area and the nonlinear least square principle are shown in Fig. 6, which shows good fitting effect of near-ground typhoon field (simulation goodness is 93.57%). The typhoon speed at the height of 10 m is large and it increases slowly with the height. For qualitative and quantitative comparison of differences between normal wind field and typhoon field, the wind speeds in the typhoon field and normal wind field on 300 m of type-A landform in the standards (GB50009-2012) was defined equal. Changes of average wind speeds in both typhoon field and normal wind field with height were expressed by the exponential wind profile

$$V = V_{10}(h/10)^{\alpha} \tag{2}$$

Where V_{10} is the average wind speed at 10min on the height of 10m, which is 14.37 m/s in the typhoon field and 13.01 m/s in the normal wind field. α is the ground roughness index. According to output results of WRF, α was 0.091 in the areas where typhoon ran through, and it was 0.12 for type-A landform in the standard (GB50009-2012). h is the height from the ground.

The calculation formula of turbulence intensity is

$$I_u = c(10/h)^{-\alpha} \tag{3}$$

Where c is the nominal turbulence intensity on 10m. According to the synchronous monitoring results to “Megi” of Hu *et al.* (2011), c was calculated 0.15. The relation curves between near-ground turbulence intensity in the center of simulation area and height in both typhoon field and normal wind field are shown in Fig. 5. It can be seen from Fig. 5 that the numerical value of turbulence intensity on the same height in the typhoon field is significantly higher than that in type-A normal wind field.

3. Mesoscale/small-scaled coupling simulation method

3.1 Brief introduction to the project

Main structural design parameters and model structure of the 5MW wind turbine with a horizontal axis and three blades in a wind field in southeastern coast in China are listed in Table 2. The tower was a structure with fixed length and varying thickness. The thickness at top and bottom were 40 mm and 90 mm, respectively. The dip angle and cut-out wind speed of blades were 5° and 25 m/s, respectively. The included angle between any two blades was 120° and all blades were in uniform distribution along the circumferential direction. Lengths of blades were 60 m. Detailed parameters of blade element section along the wingspan are shown in Table 3. The vertical downward blade of the wind turbine was defined Blade A and the rest two blades were defined Blade B and Blade C along the clockwise rotation. The cabin size was 18 m (Length) × 6 m (Width) × 6 m (Height). Tower, blade and cabin were solid model of large wind turbine was formed by Boolean operation.

3.2 Setting of working conditions

Size of sand particles was set 0.10 mm and 0.25 mm in the maximum statistical probability interval (Jiang *et al.* 2010) as well as 1mm under the extreme working conditions. A total of 6 working conditions of typical wind speed and size of sand particles under “Megi” and type-A landform were set (Table 4). Influences of wind-sand extreme conditions under strong typhoon on aerodynamic performance of the wind turbine system were compared.

3.3 Wind-sand coupling movement governing equation

3.3.1 Particle transportation equation

Compared with the air inflow viewed as a continuous phase, sand particles accounted for a small proportion in air. The volume fraction of sand particles in air was still far lower than 10% in ultra-strong sand storm (wind speed ≥25 m/s). Based on similar practices, DPM has been extensively in studying multi-phase flow combination. In the present study, DPM was intervened into the continuous phase to

Table 2 Main structural design parameters and model structure of the 5MW large wind turbine

Parameter	Numerical values	3D model of blade	3D model of wind turbine
Tower height	124 m		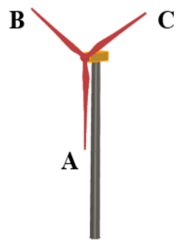
Radius at top	3.0 m		
Radius at bottom	3.5 m		
Thickness at top	0.04 m		
Thickness at bottom	0.09 m		
Blade length	60 m		
Cabin size	18 m×6 m×6 m		

Table 3 Parameters of blade of the wind turbine

Position/%	Spanwise/m	Chord length /m	Inflow angle/°	Pitch angle of blade element /°	Position/%	Spanwise/m	Chord length /m	Inflow angle/°	Pitch angle of blade element /°
5	3	2.90	0.823	37.140	55	33	1.95	0.169	-0.293
10	6	3.66	0.640	26.672	60	36	1.75	0.156	-1.072
15	9	4.41	0.507	19.069	65	39	1.58	0.144	-1.736
20	12	4.56	0.414	13.692	70	42	1.42	0.134	-2.310
25	15	4.25	0.346	9.830	75	45	1.27	0.125	-2.810
30	18	3.91	0.296	6.976	80	48	1.12	0.118	-3.250
35	21	3.59	0.258	4.802	85	51	0.98	0.111	-3.640
40	24	3.05	0.229	3.103	90	54	0.83	0.105	-3.987
45	27	2.63	0.205	1.742	95	57	0.69	0.099	-4.299
50	30	2.29	0.186	0.630	100	60	0.54	0.095	-4.580

Table 4 Working conditions for wind-sand coupling computation of wind turbine

Size of sand particles (mm)	Wind field	
	"Megi"(14.37 m/s)	Type-A(13.01 m/s)
0.10	Working condition 1	Working condition 4
0.25	Working condition 2	Working condition 5
1.00	Working condition 3	Working condition 6

3.3 Wind-sand coupling movement governing equation

3.3.1 Particle transportation equation

Compared with the air inflow viewed as a continuous phase, sand particles accounted for a small proportion in air. The volume fraction of sand particles in air was still far lower than 10% in ultra-strong sand storm (wind speed ≥25 m/s). Based on similar practices, DPM has been extensively in studying multi-phase flow combination. In the present study, DPM was intervened into the continuous phase to make wind-sand two-way coupling (Liu *et al*. 2017, Douvi and Margaris 2012) operation after the calculation stabilization of wind field. The movement equilibrium equation of sand particles in the wind field is

$$\frac{d\vec{u}_p}{dt} = F_D(\vec{u}-\vec{u}_p) + \frac{\vec{g}(\rho_p-\rho)}{\rho_p} + \vec{F} \tag{4}$$

Where $\vec{u}_p$ is the speed of discrete-phase particles. $\vec{u}$ is the speed of continuous-phase fluid. $F_D(\vec{u}-\vec{u}_p)$ is the drag force of unit mass. ρ_p and ρ are particle and fluid densities. $\vec{F}$ is the interaction force between the discrete phase and continuous phase, where

$$F_D = \frac{18\mu}{\rho_p d_p^2}\frac{C_D R_e}{24} \tag{5}$$

Where μ is the viscosity coefficient of fluid. d_p is the diameter of particle. Re is the relative Reynolds number and it can be expressed as

$$Re = \frac{\rho d_p |u_p - u|}{\mu} \tag{6}$$

With considerations to effects of discrete-phase sand particles, the continuous-phase basic governing equations of wind can be expressed as

$$\frac{\partial \rho}{\partial t} + \nabla\cdot(\rho\vec{u}) = S_m \tag{7}$$

$$\frac{\partial}{\partial t}(\rho\vec{u}) + \nabla\cdot(\rho\vec{u}\vec{u}) = -\nabla p + \nabla\cdot(\bar{\tau}) + \rho\vec{g} + \vec{F} \tag{8}$$

Where S_m is the second discrete-phase mass when the continuous phase is added. p is the pressure. $\bar{\tau}$ is the tensor of stress. $\rho\vec{g}$ is the gravity. Among them, $\bar{\tau}$ can be expressed as

$$\bar{\tau} = \mu[(\nabla\vec{u} + \nabla\vec{u}^T) - \frac{2}{3}]\nabla\vec{u}I \tag{9}$$

Where I is the unit tensor. The second item in the right of the equation refers to the volume expansion.

3.3.2 Particle impact model

The impact process of sand particles onto the surface of wind turbine obeys to the law of conservation of momentum. The key of solving impact force lies in the impact time. Based on consideration of engineering safety, possible fractures of sand particles in the impact process were neglected in the calculation. It was believed that the interaction between sand particles and structure obeys to Newton's second law and hypothesized (Coelho 2018, Brunt M. and Brunt G. 2013) that the speed after rebounding was consistent with that before the impact. According to the theorem of momentum

$$\int_0^\tau f(t)dt + \int_{v_s}^{-v_s} mdv = 0 \tag{10}$$

Where $f(t)$ is the impact force vector of single sand particle (N) and v_s is the speed vector of sand particles.

The impact force of sand particles onto the structure in unit time $F(\tau)$ is

$$F(\tau) = \frac{1}{\tau}\int_0^\tau f(t)dt = \frac{2mv_s}{\tau} \tag{11}$$

Sand particles impacting on the wind turbine were viewed as spheres approximately

$$F(\tau) = \frac{2mv_s}{\tau} = \frac{1}{3\tau}\rho\pi D_p^3 v_s \tag{12}$$

Since diameter of sand particles was 1mm and lower and the final horizontal speed before the impact was large, the wind turbine surface could be simplified as an infinite large plane (Robberg *et al*. 1965). The collision time (τ) is

$$\tau = 1.47\left[\left(\frac{5m}{4n_1}\right)^{2/5}\frac{1}{v_s^{1/5}}\right]\left(1+\frac{1}{\varphi^{1/5}}\right) \tag{13}$$

$$n_1 = \frac{4\sqrt{R}}{3\pi\left(k_1+k_2\right)} \tag{14}$$

Where m is the mass of sand particles and φ is the recovery coefficient (φ=1). Value of k is related with sand particles and material properties of wind turbine.

Then, the impact force of sand particles on the structure can be simplified as

$$F(\tau) = \frac{1}{3\tau}\rho\pi D_p^3 v_s \tag{15}$$

3.4 Setting of computational domain

To assure full development of wake flow of wind turbine, the computational domain size was set 12D×5D×5D (flow direction X× spanwise direction Y× vertical direction Z, where D is the diameter of wind wheel). The wind turbine was put at the entrance 3D away from the computational domain (Fig. 7). With considerations to computational efficiency and accuracy, the distort complexity of blade surface was taken into account and the discrete hybrid gridding was applied. The whole computational domain was divided into locally encrypted region and peripheral region. The former one contained the wind turbine model and used s non-structural gridding. The later one had a regular shape and applied the high-quality structural gridding.

To assure reliability of the numerical simulation results, grid independent verification was carried out to determine the optimal gridding scheme. Grid quality and wind pressure coefficient on the windward surface under different gridding schemes are listed in Table 5. With the increase of total number of grids, the grid quality is increased, while the grid skewness and wind pressure coefficient of the windward surface are decreased gradually. The grid quality under 8.4 million of grids and 11 million of grids were similar with calculated results. With comprehensive consideration to computational accuracy and efficiency, the gridding scheme involving 8.4 million of grids was chosen. The computational domain and specific gridding schemes are shown in Fig. 7.

Calculation parameters and setting of boundary conditions are listed in Table 6. In this study, k-ε model was applied. Numerical values were calculated by 3D single accuracy and separated solver. Flow rate in the flow field was an absolute value and the air model was equivalent to an ideal incompressible fluid. Under different working conditions, entrances of the computational domain applied the wind profile models of typhoon and normal wind, respectively. During flow field solving, SIMPLEC algorithm was applied to realize coupling between speed and pressure. The solving format of convective term was second-order. In the calculation process, grid tilt correction was set to increase calculation effect of hybrid grids. The calculation residual error of the governing equation was set 1×10^{-6}. The left and top boundary conditions of the computational domain were set speed entrances, while the right was pressure outlet and walls were symmetric slip-free walls. Details are shown in Fig. 7(a).

Fluid parameters of typhoon and normal wind field, such as average wind profiles, turbulence intensity, turbulence kinetic energy, turbulence integral scale and specific dissipation rate, were defined by using the user defined function (UDF) document. The above air model was integrated into the Fluent software (Fig. 8) to numerical simulation of wind-sand coupling movement caused by strong typhoon under mesoscale and small-scaled embedding conditions.

3.5 Validity verification of wind field simulation

Comparison curves between UDF settings and near-front average wind speed and turbulence profile of the wind turbine are shown in Fig.9.Clearly, near-front average wind speed and turbulence profile of the wind turbine conform well to inlet condition in UDF setting. The average field becomes stable.

Moreover, the horizontal plane of the lowest point that the blade tip scans was used as the boundary surface according to interference of tower from the upstream blade tail.

The tower was divided into non-disturbed section (height: 0 ~ 64 m) and disturbance section (height: 64 ~ 124 m). In the non-disturbed section, wind pressure distributes typical around a cylinder. The pressure coefficient distribution curve along circumferential distribution is

Table 5 Working conditions for wind-sand coupling computation of wind turbine

Gridding schemes	I	II	III	IV	V
Number of grids	1.05 million	5 million	7 million	8.4 million	11 million
Grid quality	0.11	0.35	0.48	0.59	0.61
Grid skewness	0.96	0.85	0.80	0.75	0.73
Wind pressure coefficient on windward surface	1.1	0.96	0.91	0.85	0.83

Table 6 Calculation of parameters and boundary conditions

Calculation parameters	Parameter setting	Calculation parameters	Parameter setting
Inlet	Velocity inlet	Turbulence model	*k-ε*
Outlet	pressure outlet	Discretion of pressure term	Standard format
Walls	Non-Slippling walls	Transient equation	Second-order implicit expression
Other boundary conditions	Symmetric boundary conditions	Convergence tolerance	10^{-6}
Flow field solving method	SIMPLEC	Turbulent kinetic energy	Second-order windward format

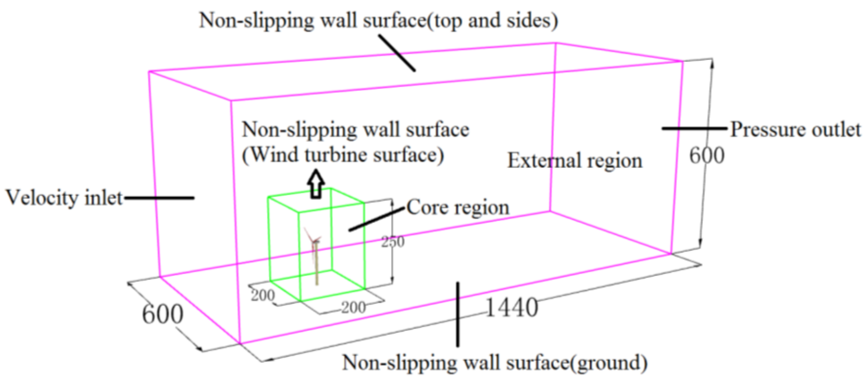

(a) Overall gridding

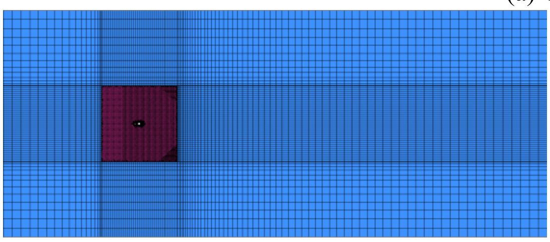

(b) Gridding of the x-y plane

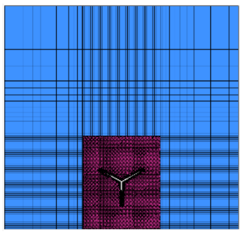

(c) Gridding of the y-z plan

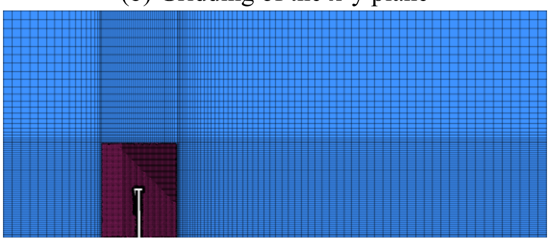

(d) Gridding of the x-z plan

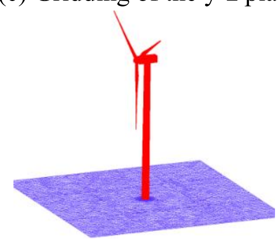

(e) Gridding of the encrypted region

Fig. 7 Computational domain and gridding scheme

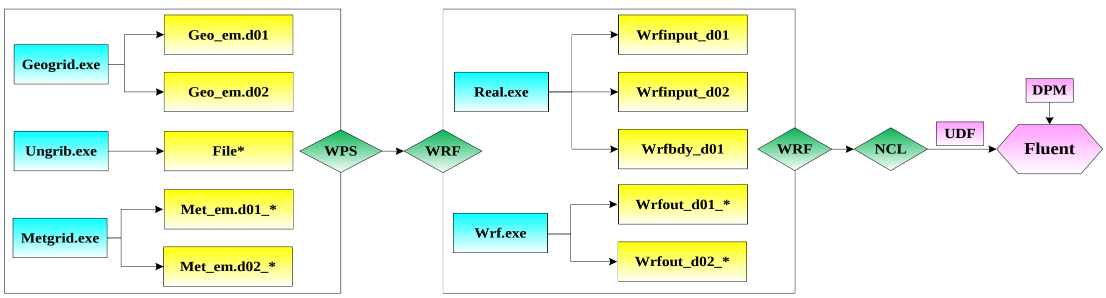

Fig. 8 Procedure of WRF/CFD coupling computation and embedding

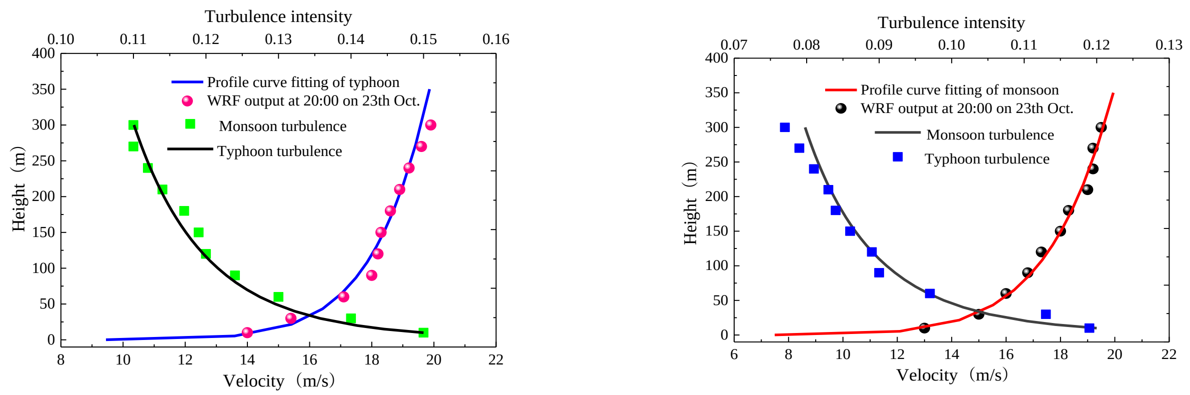

(a) Typhoon (b) Normal wind

Fig. 9 Velocity and turbulence profile

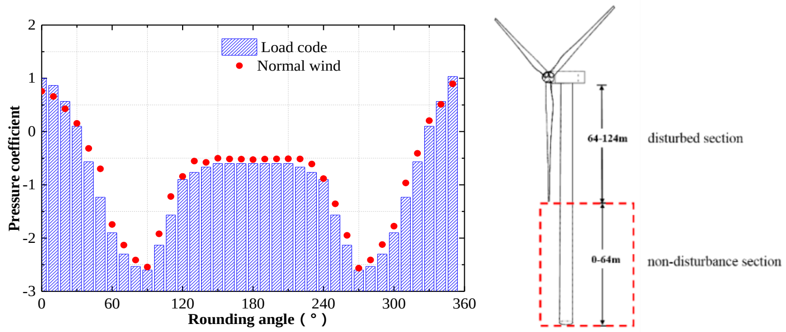

Fig. 10 Typical section of tower and distribution curves of standard wind pressure

shown in Fig. 10 and it is compared with standard numerical values (GB50009-2012). It can be known from analysis that numerical simulated and standard pressure coefficients present consistent circumferential distribution pattern and numerical values. The simulated value is slightly smaller than the standard value on leeward zone, indicating that the simulation of normal wind field meets requirements.

4. Flow field analysis

4.1 Characteristics of flow around

The speed flow line and turbulence energy distribution on the typical height section of the wind turbine tower under normal wind and typhoon effects are shown in Fig. 11 and Fig. 12, where H is the height of tower. According to analysis, the speed flow line under loading conditions generally present similar distribution. However, the wind speeds surrounding the tower and blades of the wind turbine in typhoon field are higher than those in normal wind field. Incoming flows all split at 0° on the windward surface of the tower, thus producing backflows and different scales of eddies on the leeward surface of the tower. Moreover, incoming flows move by attaching on the blade surface and thereby form small-scaled eddies on the leeward surface of blade after passing through the front and rear edges of the blades. Turbulence energy surrounding the tower in the typhoon field is slighter higher than that in normal wind field. The interaction between blades and tower on the upper middle position of the tower is significant in the typhoon field.

4.2 Wind pressure distribution

The pressure coefficient distribution curves of the wind turbine tower in the normal wind field and typhoon field are shown in Fig. 13. The circumferential pressure coefficient of wind turbine tower under two loading conditions presents a symmetric distribution along the windward surface. Moreover, it decreases firstly and then increases with the increase of rounding angle until reaches a steady development close to the leeward region. The negative pressure zone on crosswind surface of the tower in the typhoon field is slightly larger than that in the normal wind field slighter higher than that in normal wind field. The interaction between blades and tower on the upper middle position.

Pressure coefficient clouds on windward surface and leeward surface of blades of the wind turbine and its mean along the spanwise direction under two loading conditions are shown in Fig. 14. The distribution curves of overall pressure coefficients of blades of wind turbine under low loading conditions are shown in Fig. 15. It can be seen from Figs. 14 and 15 that: 1) the pressure coefficient on windward surface of blades is basically positive under two loading conditions. Negative pressure coefficient only occurs in front edge of blade and trailing edge of blade root. However, pressure coefficient on leeward surface of blades

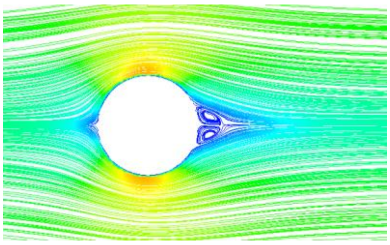
(a) Normal wind (0.3H)

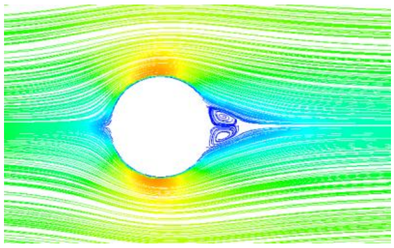
(b) Typhoon (0.3H)

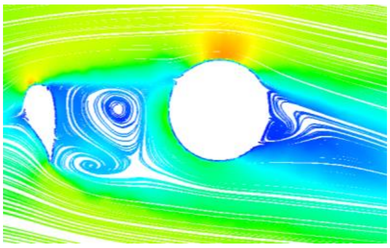
(c) Normal wind (0.8H)

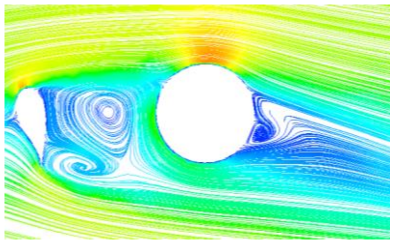
(d) Typhoon (0.8H)

Fig. 11 Speed flow line on the typical height section of the wind turbine tower

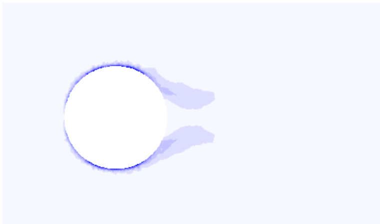
(a) Normal wind (0.3 H)


(b) Typhoon (0.3 H)

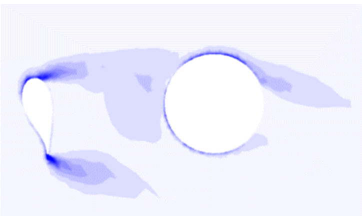
(c) Normal wind (0.8 H)

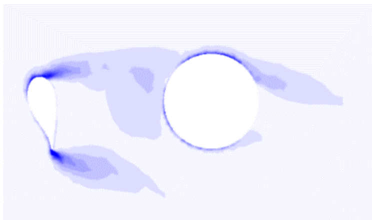
(d) Typhoon (0.8 H)

Fig. 12 Turbulence energy distribution on the typical height section of the wind turbine tower

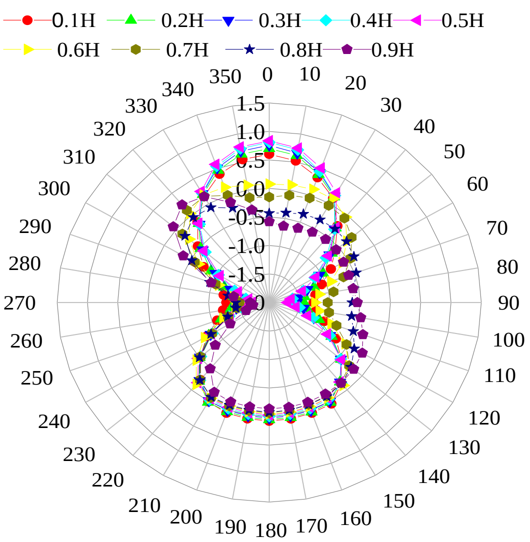

(a) Normal wind

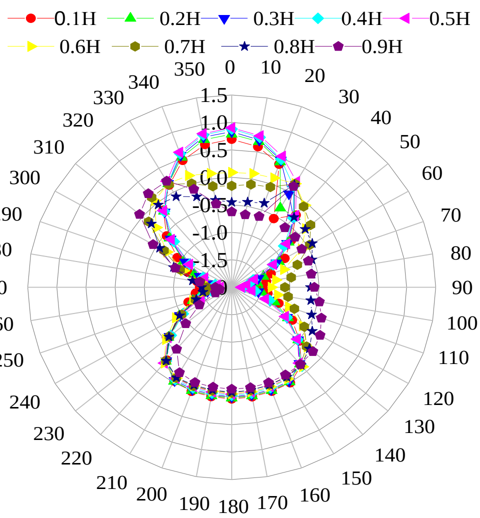

(b) Typhoon

Fig. 13 Wind pressure coefficient distribution on the wind turbine tower

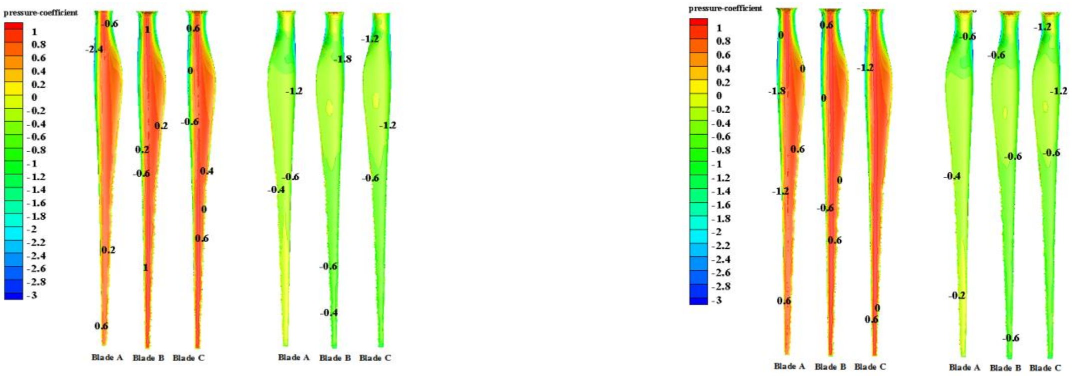

(a) Normal wind (b) Typhoon

Fig. 14 Pressure coefficient distribution cloud on blades

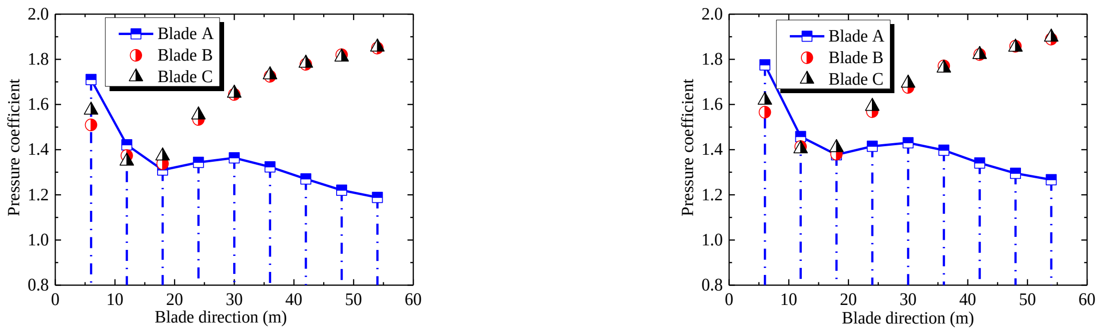

(a) Normal wind (b) Typhoon

Fig. 15 Distribution curves of wind pressure coefficient along blade span

is basically negative. 2) The positive pressure on windward surface of Blade A generally increases along the spanwise direction, whereas the positive pressure on windward surfaces of Blade B and Blade C changes slightly along the spanwise direction, without significant regulations. Negative pressure on leeward surface of all blades decreases firstly and then increases along the spanwise direction. In general, the overall pressure coefficient of all blades decreases firstly and then increases along the spanwise direction. The overall pressure coefficient of all blades in the typhoon field is higher (6.60% up to the most) than that in the normal wind field.

5. Aerodynamic distribution on tower in the wind-sand coupling environment

5.1 Distribution characteristics of sand particles

The impact behavior of sand particles in wind-sand flow field onto the wind turbine surface is easy to produce extreme load effect. To display distribution density of sand particles on different positions of the wind turbine, the trajectory of sand particles was tracked based on the horizontal speed of sand particles. Distributions of sand particles in the wind-sand field under 6 working conditions are shown in Fig. 16, in which the sand particle density is coarsened according to equal proportion.

It can be found in Fig. 16 that due to shielding effect of tower by blades, impact positions of sand particles are mainly in the height range of 0 ~ 0.6 H on the windward surface of the tower under all working conditions. Driven by airflow eddy, there are few sand particles attached on the shielded region and leeward surface of the tower. The number of sand particles collected from the tower and blades reaches the highest under working condition 4. Moreover, the number of sand particles decreases gradually with the increase of sand particle size.

The comparison curves of number of sand particles on the tower and blades, impact speeds and impact speed occupancy (ratio between number of sand particles in the distribution intervals of speeds and total number of sand particles) under six working conditions are shown in Fig. 17 and Fig. 18.

1) Given small size of sand particles, impact speed occupancy of sand particles on tower and blades in the typhoon field and normal wind field basically show consistent variation laws under all six working conditions. Impact speed of sand particles is generally within the range of -2.5 - 12.5 m/s. With the increase of size of sand particles, the speed distribution curves of sand particles moves toward the right gradually and the impact speed concentrates in the range of -2.5 - 17.5 m/s. When size of sand particles reaches 1mm, the impact speed of sand particles onto the tower in typhoon field is higher than that in normal wind field. However, the distribution patterns of impact speed in both typhoon

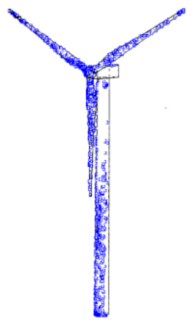
(a) Working condition 1

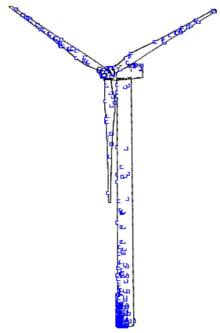
(b) Working condition 2

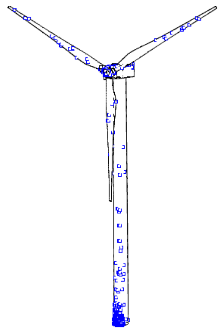
(c) Working condition 2

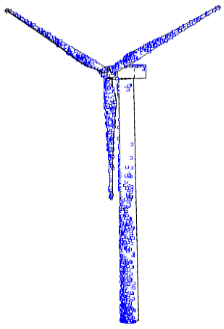
(d) Working condition 2

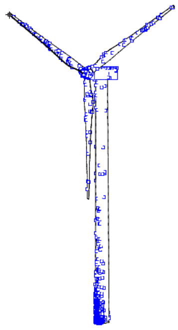
(e) Working condition 2

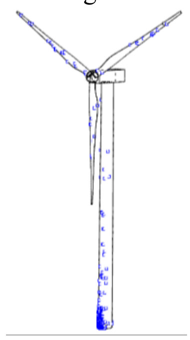
(f) Working condition 2

Fig. 16 Distributions of sand particles in the wind-sand field

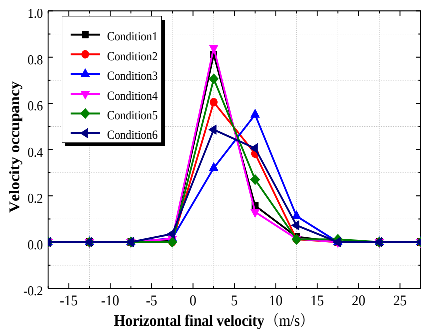

(a) Tower

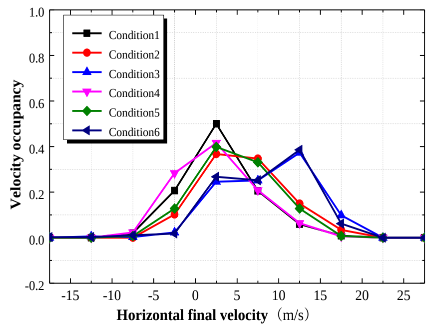

(b) Blades

Fig. 17 Distribution curves of impact speed occupancy of sand particles

field and normal wind field are consistent.

2) The number of sand particles collected from wind turbine tower and blades under normal wind is higher than that under typhoon. Meanwhile, the quantity of sand particles decreases significantly with the increase of sand particle size. Under coupling effect between large sand particles and wind field (working conditions 3 and 6), the mass distribution of sand particles on wind turbine surface in unit time is relatively large.

5.2 Sand-induced loads

Sand-induced loads on the wind turbine under 9 working conditions were calculated by the Eq. (15). Meanwhile, sand-induced load, wind-induced load and sand-wind load ratio of the tower on different heights are shown in Fig. 19, Fig. 20 and Table 7. According to comparison:

1) The incoming wind field influences sand-induced load distribution on the tower surface of the wind turbine significantly. Extreme sand-induced loads are produced in the height range of 0 ~ 0.05 H. The sand-wind load ratio in the height range of 0 ~ 0.05 H reaches 3.937% under the working condition 3 (typhoon +1 mm).

2) The impact loads of small sand particles onto the tower distribute uniformly on different height in both normal wind field and typhoon field. Blade A can shield large sand particles significantly. The impact loads of large sand particles drop quickly in the disturbance section of the tower.

3) Wind-induced load distributions on tower surface in typhoon field and normal wind field are relatively consistent. Specifically, wind-induced loads increase firstly, then decrease and finally increase along the meridian direction. The maximum wind-induced load on the non-disturbance section of the tower in typhoon field is 14.72% higher than that in normal wind field.

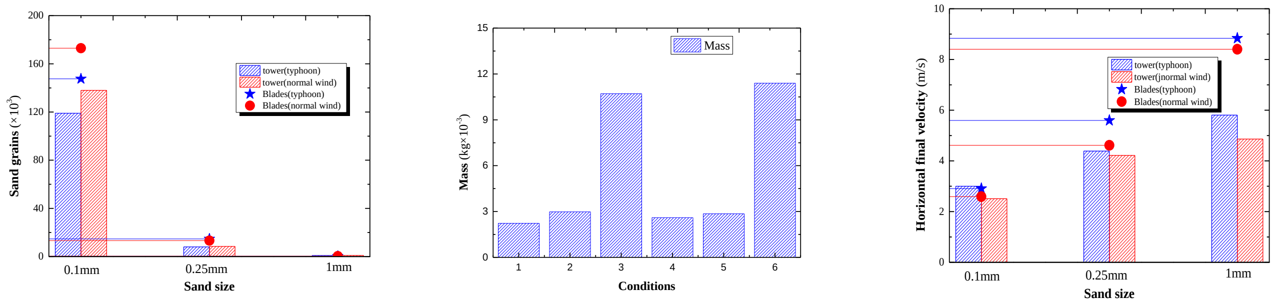

(a) Number of sand particles (b) Mass distribution (c) Horizontal final velocity

Fig. 18 Number of sand particles on the wind turbine and speed distribution curves

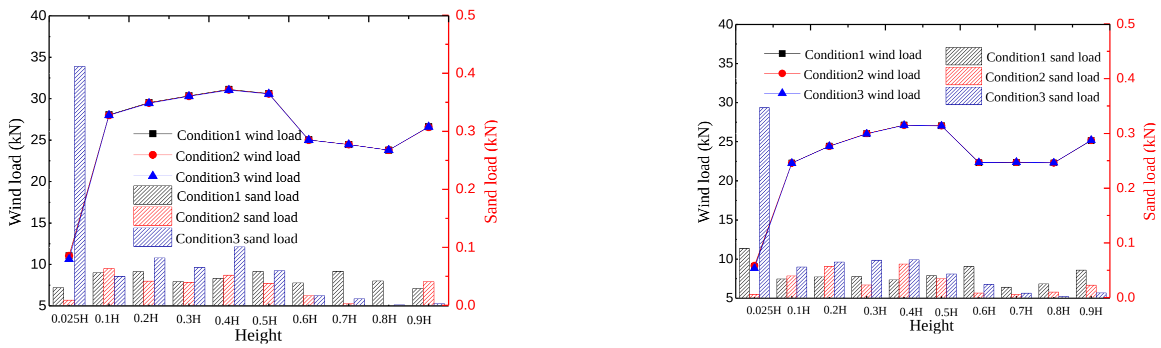

(a) Typhoon (b) Normal wind

Fig. 19 Wind-induced load and sand-induced load distribution curves along meridian directions

Table 7 Wind-sand load ratio (‰) in different height ranges of the tower structure under working conditions 1 ~ 6

Height	Working conditions					
	Typhoon			Monsoon		
	1	2	3	4	5	6
0.00~0.05 H	2.76	0.80	39.37	9.90	0.66	38.75
0.05~0.15 H	2.00	2.26	1.78	1.53	1.78	2.51
0.15~0.25 H	1.97	1.41	2.78	1.55	2.33	2.66
0.25~0.35 H	1.35	1.30	2.15	1.48	0.89	2.62
0.35~0.45 H	1.49	1.67	3.25	1.20	2.26	2.55
0.45~0.55 H	1.90	1.23	1.95	1.49	1.28	1.59
0.55~0.65 H.	1.54	0.66	0.66	2.55	0.37	1.08
0.65~0.75 H	2.39	0.12	0.46	0.84	0.26	0.36
0.75~0.85 H	1.76	0.00	0.03	1.13	0.45	0.09
0.85~0.95 H	1.09	1.53	0.10	2.00	0.90	0.35

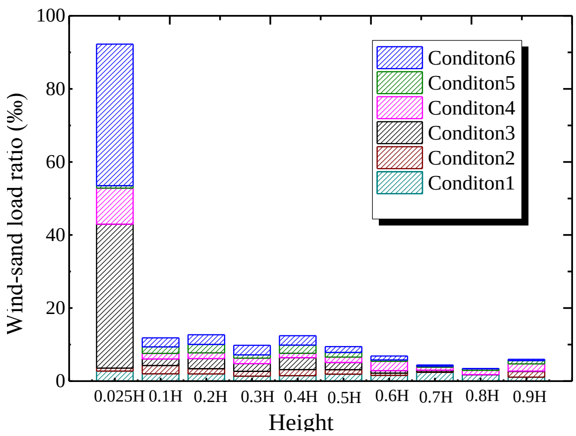

Fig. 20 Wind-sand load ratio of the wind turbine under working conditions 1 - 6

5.3 Contrast analysis of pressure coefficient

For quantitative comparison of surface pressure distribution at different stop position, and-induced pressure coefficient and equivalent pressure coefficient were defined for a quantitative comparison of pressure distributions on tower surface under different halting positions of the wind turbine. Details are introduced by Eq. (16) ~ (18) in the revised manuscript. The equivalent idea is: ① impact loads of sand particles at different monitoring points of the surface were transformed into sand-induced pressure intensity; ② the ratio between sand-induced pressure at monitoring points and wind pressure at the corresponding reference height was calculated, which is known as the sand pressure coefficient; ③ the wind pressure coefficient and

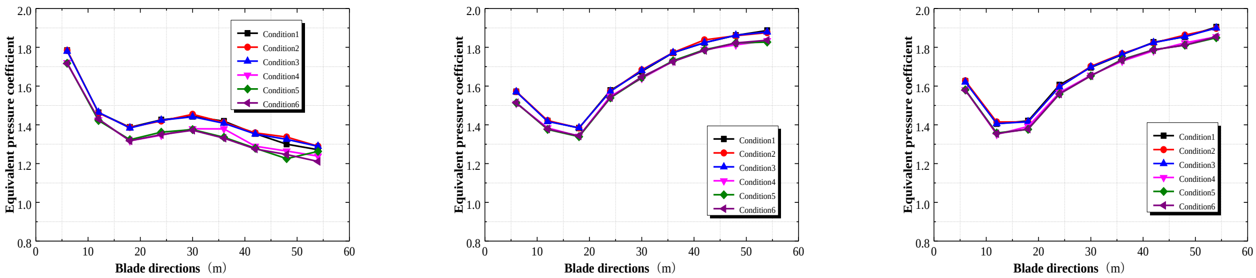

(a) Blade A (b) Blade B (c) Blade C

Fig. 21 Equivalent pressure coefficient of blades

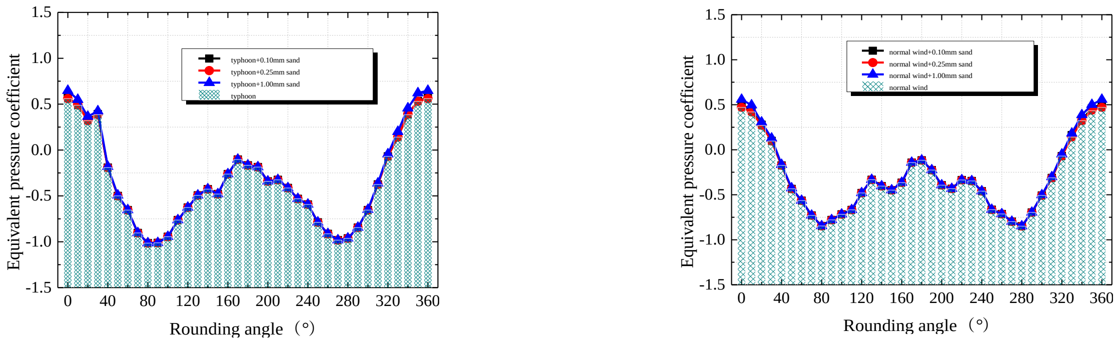

(a) Typhoon (b) Normal wind

Fig. 22 Equivalent pressure coefficient on the 0.025 H section (3.2 m) of tower

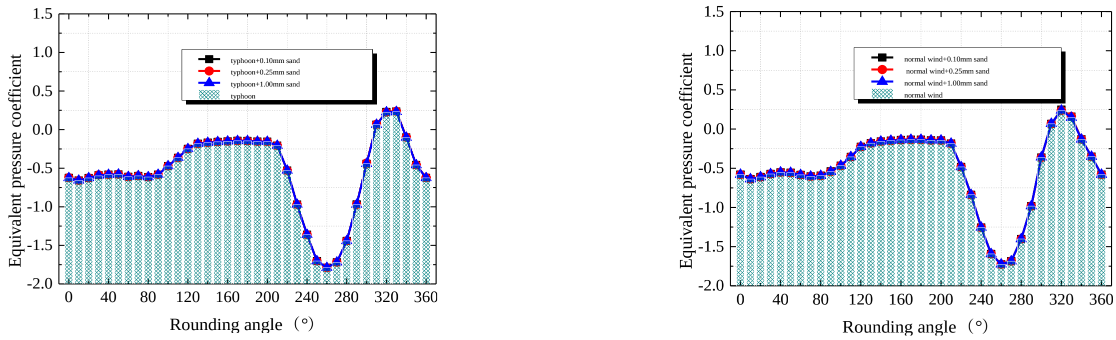

(a) Typhoon (b) Normal wind

Fig. 23 Equivalent pressure coefficient on the 0.90 H section (111.6 m) of tower

the transformed sand-induced pressure coefficient are added, and the equivalent pressure coefficient is gained. The equivalent pressure coefficient can be viewed as an equivalent goal. The wind-sand coupling effects on the tower of wind turbine under different halting positions were quantified and compared.

$$C_{pi} = \left(P_i - P_H\right) / 0.5\rho V_H^2 \tag{16}$$

$$C_{psi} = \frac{nF(\tau)}{S} / 0.5\rho V_H^2 \tag{17}$$

$$C_{pei} = C_{psi} + C_{pi} \tag{18}$$

Where C_{pi} is the average wind pressure coefficient at point i. P_i is the average pressure at measuring points on the height of Z, (Pa). PH is the static pressure in far front on the reference height, (Pa). ρ is air density and it determines 1.225 kg/m^3 in this study. V_H is the average wind speed in far front on the reference height. C_{psi} is the sand-induced pressure coefficient at point i. n is the number of sand particles impacting on a region in unit time. $F(\tau)$ is the impact force of single sand particle to the structure. S is the area of computation area. C_{pei} is the equivalent pressure coefficient at point i. Considering distribution characteristics of sand particles and the aerodynamic interference effect between blade and tower, the sand-induced effect is studied by choosing the non-disturbance section 0.025H and the disturbance section 0.9H as the typical section. In addition, the equivalent pressure coefficient of blades of wind turbine is given.

The comparison curves of equivalent pressure coefficients of Blade A, B and C under different working

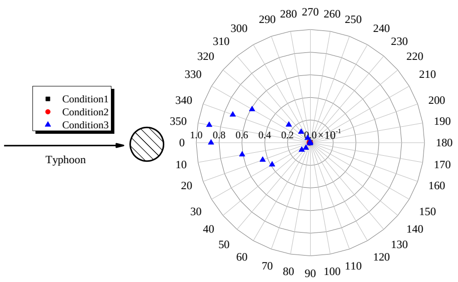

(a) Typhoon

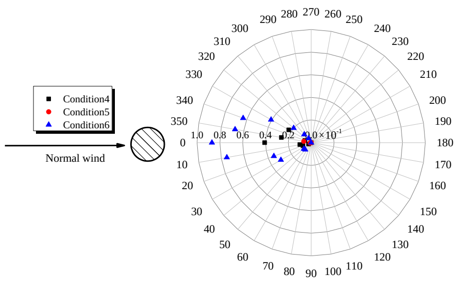

(b) Normal wind

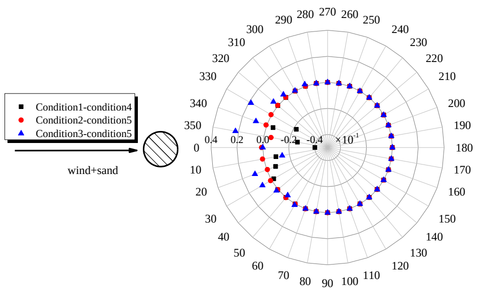

(c) Differences of sand-induced pressure coefficients in typhoon and normal wind fields under equal particle size

Fig. 24 Sand-induced pressure coefficient on the 0.025 H section (3.2 m) of tower

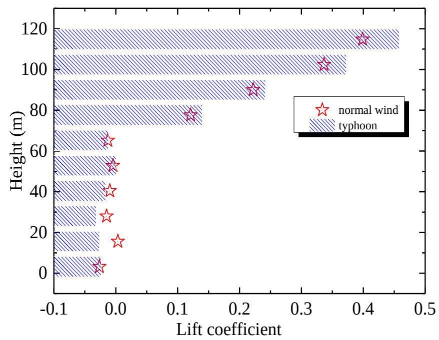

(a) Lift coefficient

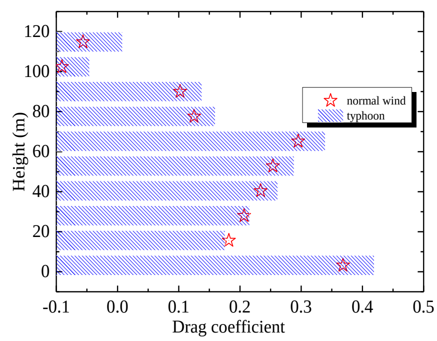

(b) Drag coefficient

Fig. 25 Distribution curves of lift coefficient and drag coefficient of the tower in normal wind field and typhoon field

conditions are shown in Fig. 21. Based on analysis, the distribution law and numerical value of equivalent pressure coefficients of three blades under the same incoming flow are basically consistent. The equivalent pressure coefficient of Blade A decreases firstly, then increases and finally decreases along the spanwise direction. The equivalent pressure coefficient of Blades B and C decreases firstly and then increases along the spanwise direction. The equivalent pressure coefficient of all blades in the typhoon field is about 6.43% higher to the maximum extent compared with that in normal wind field

The comparison curves of equivalent pressure coefficient on two typical sections in the typhoon field and normal wind field are shown in Fig. 22 and Fig. 23. According to analysis,

1) The circumferential wind pressure coefficient on the non-disturbance section in the normal wind field is symmetric under all working conditions. The equivalent pressure coefficient on the leeward surface of the tower in the typhoon field fluctuates slightly. However, the circumferential surface pressure coefficient on the disturbance section (0.90 H) is not symmetric. There are negative pressures in the center of windward surface of the tower. Moreover, the pressure distribution presents the same law under different incoming conditions.

2) The pressure coefficient in the range of 0 ~ 30° at two sides of the windward surface on the 0.025 H section differs significantly in the typhoon field and normal wind field. The equivalent pressure coefficients under working condition 3 and 6 are higher than those under rest working conditions. This reflects that large sand particles are easy to cause significant impact loads on the tower. The shielding effect of blades weakens the impact of sand particles on the disturbance section significantly

There’s an evident separation of numerical value of the equivalent pressure coefficient on windward surface on the non-disturbance section (0.025 H). For quantifying sand-induced effect, the sand-induced pressure coefficient distribution curves on the non-disturbance section (0.025 H) are drawn (Fig. 24). In the typhoon field and normal wind field, large sand particles impact on the tower more

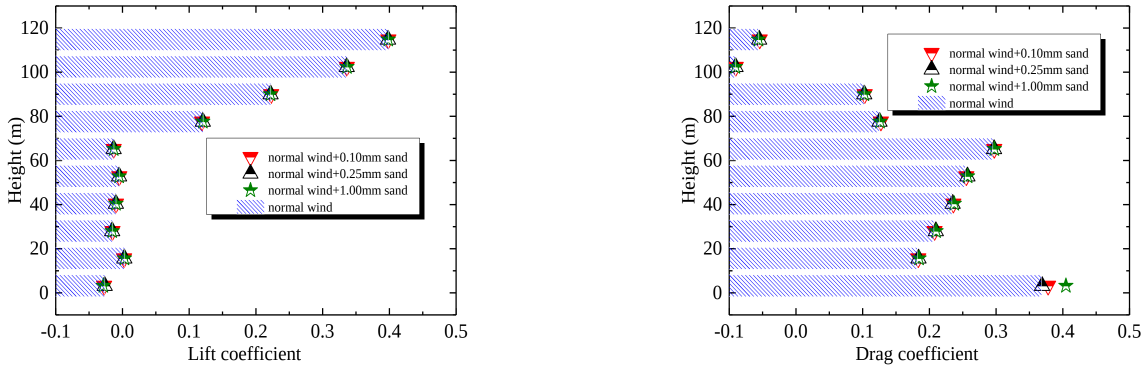

(a) Lift coefficient (b) Drag coefficient

Fig. 26 Distribution curves of lift coefficient and drag coefficient of the tower in the normal wind-sand coupling environment

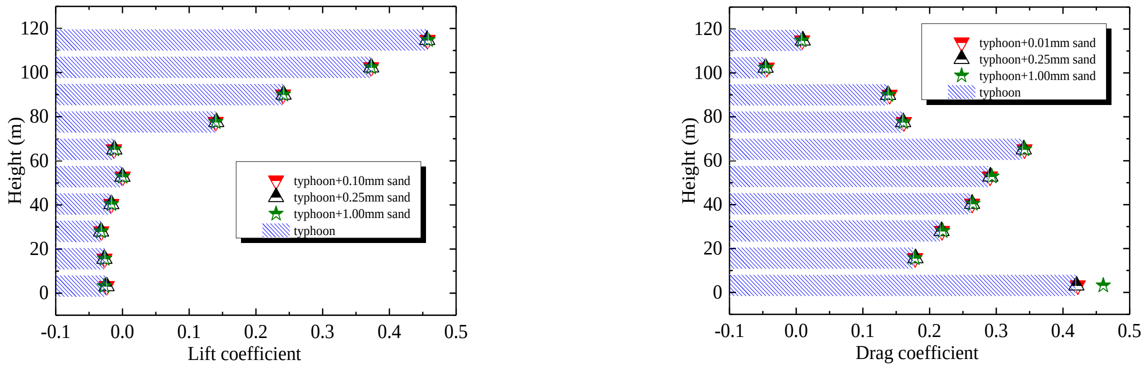

(a) Lift coefficient (b) Drag coefficient

Fig. 27 Distribution curves of lift coefficient and drag coefficient of the tower in the typhoon-sand coupling environment

strongly. The sand-induced pressure coefficient of the tower mainly concentrates in the range of 30° at two sides of the windward surface. The maximum wind-induced sand pressure coefficient in strong typhoon field is 0.09, which is 3.44% higher than that in the normal wind field.

5.4 Contrast analysis of lift and drag coefficients

Distribution curves of lift coefficients and drag coefficients on different heights of the tower in the typhoon field and normal wind field are shown in Fig. 25, Fig. 26 and Fig. 27. The calculation formulas of the crosswind lift coefficient (C_L) and downwind drag coefficient (C_D) on the tower are (Ke *et al*. 2016)

$$C_L = \frac{\sum_{i=1}^{n} C_{Pi} A_i \sin\theta_i}{A_T} \tag{19}$$

$$C_D = \frac{\sum_{i=1}^{n} C_{Pi} A_i \cos\theta_i}{A_T} \tag{20}$$

Where C_{pi} is the average wind pressure coefficient at the measuring point i of the tower. A_i is the coverage area of pressure at the measuring point i. θ_i is the included angle between the pressure at the measuring point i and the wind axis. A_T is the projection area of the overall structure along the wind axis. Based on above figures, it can get:

1) The lift coefficient of tower in the typhoon field and normal wind field increases gradually along the meridian direction. The shielding effect of blades is extremely significant at the top of tower, manifested by the sharp reduction of drag coefficient of the tower. The lift coefficient on the non-disturbance section in the normal wind field is higher than that in the typhoon field. However, typhoon increases the drag coefficient of the tower generally.

2) The drag coefficient at tower bottom is very sensitive to the impact effect of large sand particles. Under wind-sand two-phase coupling effect, the resistance coefficient of the tower structure under working condition 3 (typhoon +1 mm sand particles) is 9.80% higher than that under typhoon and it is even 13.79% higher than that under working condition 6 (normal wind+1 mm sand particles). Effects of middle and small sand particles can be neglected in the lift and drag coefficients of the tower in the wind-sand coupling environment.

6. Conclusions

Firstly, this study simulates the wind field of typhoon “Megi” by WRF mode. Secondly, the wind speed profile in the typhoon field is gained based on nonlinear least square fitting and it is used as the entrance condition of Fluent. Meanwhile, DPM is added to realize numerical simulation of gas-solid flows under mesoscale and small-scaled coupling effect. On this basis, aerodynamic distribution characteristics of large wind turbine under the wind-sand coupling effect induced by strong typhoon are discussed systematically. Some major conclusions could be drawn:

1) The WRF mode can simulate near-ground typhoon field effectively. Besides, the exponential of the wind profile of "Megi" is calculated0.091 by the least square fitting. In this study, the 3D typhoon field of such large flexible thin structure can be simulated effectively by downscaling method. Research results provide load input for the follow-up aerodynamic analysis.

2) Evident 3D effects of the wind field and wind pressure coefficient on the wind turbine system can be observed when only one-way wind effect are considered. Compared with the normal wind field, typhoon field intensifies the eddy falling on the leeward surface at the top of the wind turbine tower and increases the negative pressure on the leeward surface of the tower. Compared with parameters in the normal wind field, the maximum wind load on the non-disturbance section and the overall pressure coefficient of blades in the typhoon field are 14.72% and 6.60% (highest) higher.

Acknowledgments

This work was jointly funded by Natural Science Foundation of China (51878351, 51761165022), National key research and development projects (2019YFB1503701, 2017YFE0132000).

References

An Y. (2011), "Study on the performance of large double runner wind turbine against typhoon", South China University of Technology. (In Chinese)

Brunt M., Brunt, G. (2013), "Introducing conservation of momentum", *Phys. Edu*., **48**(5), 664-669.

Bagnold R.A. (1937), "The Transport of Sand by Wind", *Geograph. J*., **89**(5), 409-438.

Bagnold R.A. (1935), "The Movement of Desert Sand", *Geograph. J*., **85**(4), 342-365.

Coelho R.L. (2018), "On the deduction of Newton's second law", *ACTA Mech*., **229**(5), 2287-2290. https://doi.org/10.1007/s00707-017-2074-2.

Carvalho, D., Rocha, A., Gómez-Gesteira, M. and Santos, C.S. (2014), "WRF wind simulation and wind energy production estimates forced by different reanalyses: Comparison with observed data for Portugal", *Appl. Energy*, **117**(3), 116-126. https://doi.org/10.1016/j.apenergy.2013.12.001.

Cheng, J., Jiang, F., Xue, C. and Pang, Q. (2012), "Computational method for maximum sediment discharge and sand-carrying wind load in the prevention and treatment of wind drift sand for railway in strong wind area", *China Railway* Sci., **33**(1), 1-5.

Chou J.S. and Tu W.T. (2011), "Failure analysis and risk management of a collapsed large wind turbine tower", *Eng. Fail. Anal*., **18**(1), 295-313. https://doi.org/10.1016/j.engfailanal.2010.09.008.

Dissanayake, P., Brown, J. and Karunarathna, H. (2015), "Impacts of storm chronology on the morphological changes of the Formby beach and dune system, U.K.", *Nat. Haz. Earth Syst. Sci. Discuss*., **15**(7), 2565-2597.

Douvi, E and Margaris, D. (2012), "Aerodynamic performance investigation under the influence of heavy rain of a NACA 0012 airfoil for wind turbine applications", *Int. Rev. Mech. Eng*., **6**(6).

Gao, G., Zhang, Y., Zhang, J., Xie, F., Zhang, Y. and Wang, J. (2018), "Effect of bogie fairings on the snow reduction of a high-speed train bogie under crosswinds using a discrete phase method", *Wind Struct*. **27**(4), 255-267. https://doi.org/10.12989/was.2018.27.4.255.

GB50009-2012(2012), "Load code for the design of building structures", China Building Industry Press.

Jiang, F.Q., Li, Y., Li, K.C., Cheng, J.J., Xue, C.X. and Ge, S.C. (2010), "Study on structural characteristics of Gobi wind sand flow in 100 km wind area along Lan-Xin Railway", *J. China Railway Society*, **32**(3), 105-110.

Karunarathna, H., Brown, J., Chatzirodou, A., Dissanayake, P. and Wisse, P. (2018), "Multi-timescale morphological modelling of a dune-fronted sandy beach", *Coastal Eng*., **136**, 161-171.

Ke, S., Yu, W., Wang, T., Zhao, L. and Ge, Y. (2016), "Wind loads and load-effects of large scale wind turbine tower with different halt positions of blade", *Wind Struct*., **23**(6), 559-575. https://doi.org/10.12989/was.2016.23.6.559.

Li, Z.N., Wng S.Y., Gong. B. (2017), "Wind tunnel test for impact of wind-sand flow on overall forces of low-rise building", *China Civil Eng, J*., **50**(1), 63-69.

Xin, L.G., Cheng, J.J., Chen, B.Y. and Wang, R. (2018), "The motion rule of sand particles under control of the sand transportation engineering", *Wind Struct*., **27**(4), 213-221.

Liu, S, Huang, S.H. and Li, Q.S. (2017), "3D numerical simulation of wind-driven rain on bridge deck sections based on eulerian multiphase model", *Eng. Mach*., **34**(4), 63-71. https://scholars.cityu.edu.hk/en/publications/publication(e737bce7-951f-4570-a470-0b4cdfeb4e7f).html.

Zhao, L., Yu, Z., Zhu, F., Qi, X. and Zhao, S. (2016), "CFD-DEM modeling of snowdrifts on stepped flat roofs", *Wind Struct*., **23**(6), 523-542. http://dx.doi.org/10.12989/was.2016.23.6.523.

Lian, J., Jia, Y., Wang, H. and Liu, F. (2016), "Numerical study of the aerodynamic loads on offshore wind turbines under typhoon with full wind direction", *Energies*, **9**(8), 613. https://doi.org/10.3390/en9080613.

Luo, Y., Chen, Q., Ren, D., Li, X. and Liao, Y. (2016), "The light-weight design of tower for under typhoon wind turbine based on the typhoon control strategy", *International Conference on Sensors, Mechatronics and Automation*.

Li, L., Kareem, A., Xiao, Y., Song, L. and Zhou, C. (2015). "A comparative study of field measurements of the turbulence characteristics of typhoon and hurricane winds", *J. Wind Eng. Ind. Aerod*., **140**, 49-66. https://doi.org/10.1016/j.jweia.2014.12.008.

Maruyama, T., Tomokiyo, E. and Maeda, J. (2010), "Simulation of strong wind field by non-hydrostatic mesoscale model and its applicability for wind hazard assessment of buildings and houses". *Hydrolog. Res. Let*., **16**(4), 40-44. https://doi.org/10.3178/hrl.4.40.

Pye, K. and Blott, S.J. (2016), "Assessment of beach and dune erosion and accretion using LiDAR: Impact of the stormy 2013-14 winter and longer term trends on the Sefton Coast, U.K.", *Geomorphology*, **266**, 146-167. https://doi.org/10.1016/j.geomorph.2016.05.011.

Priestas, A.M. and Fagherazzi, S. (2010), "Morphological barrier island changes and recovery of dunes after Hurricane Dennis, St. George Island, Florida", *Geomorphology*, **114**(4), 614-626. https://doi.org/10.1016/j.geomorph.2009.09.022.

Pries, A.J., Miller, D.L. and Branch, L.C. (2008), "Identification of structural and spatial features that influence storm-related dune erosion along a barrier-island ecosystem in the Gulf of Mexico", *J. Coastal Res*., **24**(4C),168-175. https://doi.org/10.2112/06-0799.1.

Robberg, K.B. (1965), "Shock waves in elastic and elastic-plastic media", *Sci. Press*.

Song, L., Li, Q.S., Chen, W., Qin, P., Huang, H. and He, Y.C. (2012), "Wind characteristics of a strong typhoon in marine surface boundary layer", *Wind Struct*., **15**(1), 1-15.

Sun, X., Huang, D. and Wu, G. (2012), "The current state of offshore wind energy technology development", *Energy*, **41**(1), 298-312. httpsr://doi.org/10.1016/j.energy.2012.02.054.

Skamarock, W.C., Klemp, J.B., Dudhia, J., Gill, D.O., Barker, D.M. (2008), A Description of the Advanced Research WRF Version 3. Technical Report. UCAR/NCAR. http://dx.doi.org/10.5065/D68S4MVH.

Ishihara, T., Phuc, P.V., Fujino, Y., Takahara, K. and Mekaru, T. (2005), "A field test and full dynamic simulation on a stallregulated wind turbine", *The Sixth Asia-Pacific Conference on Wind Engineering (APCWE-VI)*, **48**(7), 599-612.

Utsunomiya, T., Sato, I., Yoshida, S., Ookubo, H. and Ishida, S. (2013), "Dynamic response analysis of a floating offshore wind turbine during severe typhoon event", *ASME 2013 International Conference on Ocean, Offshore and Arctic Engineering*.

Ke, S., Yu, W., Cao, J. and Wang, T. (2013), "Study on the vibration response of wind turbine tower under typhoons", *ActaEnergiae Solaris Sinica*, **34**(8), 1434-1442.

Wyszogrodzki, A.A., Miao, S. and Chen, F. (2012), "Evaluation of the coupling between mesoscale-WRF and LES-EULAG models for simulating fine-scale urban dispersion", *Atmos. Res*., **118**(3), 324-345. https://doi.org/10.1016/j.atmosres.2012.07.023.

Zhang, Y., Huang, C. and Liu, Z. (2016), "Study on erosion characteristics of wind turbine blade coating under the effect of wind and sand", *Mat. Rev*., **30**(10), 95-99.

CC